

A coaxial line architecture for integrating and scaling 3D cQED systems

C. Axline, M. Reagor, R. Heeres, P. Reinhold, C. Wang, K. Shain, W. Pfaff, Y. Chu, L. Frunzio, and R. J. Schoelkopf
Department of Applied Physics, Yale University, New Haven, Connecticut 06511, USA

(Dated: 25 April 2016)

Numerous loss mechanisms can limit coherence and scalability of planar and 3D-based circuit quantum electrodynamics (cQED) devices, particularly due to their packaging. The low loss and natural isolation of 3D enclosures make them good candidates for coherent scaling. We introduce a coaxial transmission line device architecture with coherence similar to traditional 3D cQED systems. Measurements demonstrate well-controlled external and on-chip couplings, a spectrum absent of cross-talk or spurious modes, and excellent resonator and qubit lifetimes. We integrate a resonator-qubit system in this architecture with a seamless 3D cavity, and separately pattern a qubit, readout resonator, Purcell filter and high- Q stripline resonator on a single chip. Device coherence and its ease of integration make this a promising tool for complex experiments.

I. INTRODUCTION

Engineered quantum systems are becoming increasingly complex, with single packages incorporating on the order of ten coherent elements (resonators and qubits) used to store or process quantum information¹. Tens of logical modules, or hundreds of elements, are needed to build systems capable of quantum error correction and operations with logical qubits². As they scale, these larger systems must retain the level of control and coherence of smaller systems in order to achieve scalable levels of performance.

Multiple approaches are being explored to build scalable systems using superconducting microwave circuits. Each design must grow in size and complexity to include many elements, expanding to incorporate both planar and 3D structures^{3,4}. The ultimate size of scaled systems, regardless of architecture, will likely be set by enclosure hardware and connector volume. Even fields generated from planar structures are three-dimensional, so the importance of package and interconnect design cannot be dismissed if existing systems are to be reliably expanded.

Complex circuits have highlighted some of these packaging challenges. In lithographically-patterned circuits, cross-talk and package modes can be more difficult to suppress given the presence of wirebonds, circuit board materials, isolated ground planes, and connectors⁵. Although they contain fewer loss-inducing elements, multi-cavity 3D waveguide designs may be limited by seam dissipation^{6,7}. Enclosure and connector quality become more important in scaled systems of all types. Reduced coherence from these effects can inhibit expansion in its current form.

We aim to create a platform for system expansion in which many lithographically-defined elements can be coherently combined. To incorporate the longest-lived resources available to cQED, we would also like to add 3D cavities in a lossless manner. This coherent complexity could pave the way for error-correctable modules^{8,9}.

Cavity resonators constitute a good platform from which to reach this goal. Here, the cavity and the en-

closure are one and the same, providing a well-controlled spectrum of modes. Transmon qubits in 3D cavities have shown exceptionally high coherence^{10,11}. These cavities can be made seamless to limit dissipation while remaining integrable¹². These features form the basis for a low-loss enclosure suited to expansion.

Here we demonstrate a carefully engineered 3D waveguide package for cQED devices. By enclosing chip-based circuit elements in such a package, the resulting coaxial transmission line (“coax-line”) device can be highly coherent and extendable. Addressing a host of likely losses within the package, including coupling, seams, and materials, we produce chip-based element single photon relaxation rates at the level of the state of the art ($\sim 50 \mu\text{s}$). Resonators, qubits, and filters are fabricated on a single chip. We find that coupling between these elements can be well-controlled by changes in circuit parameters set with lithographic precision. Finally, we integrate this system with millisecond 3D cavities and show that the combined systems remain highly coherent. In the near-term, this platform allows for significantly more complex many-resonator, many-qubit circuits. When combined with more advanced techniques for fabricating 3D enclosures using lithography and multi-wafer bonding⁴, the coax-line provides an attractive route towards long-term scaling.

II. DESIGN AND PERFORMANCE

We design and measure circuits placed in 3D enclosures that avoid many common forms of loss in cQED systems. A seamless circular waveguide forms the package enclosure and acts as a ground plane (Figure 1a). Circuit elements are patterned on a sapphire substrate to define each mode of the device. Deposited and machined metals are both chosen to be aluminum. Where no metal is present on-chip, the waveguide attenuates signals below its cutoff frequency (typically 40 GHz). The chip is suspended within the enclosure by clamps at each end, where the fields from critical circuit elements are

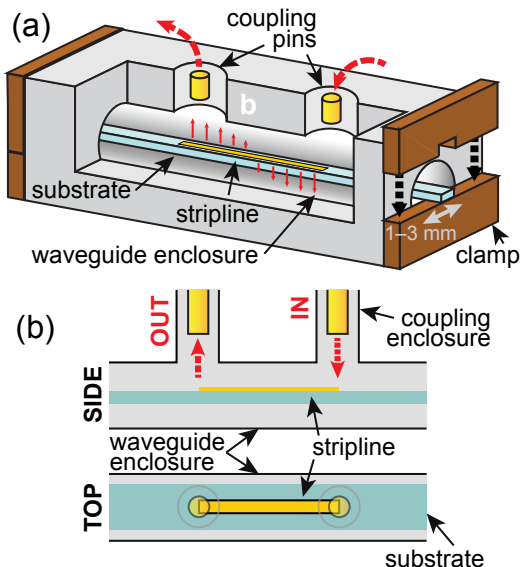


FIG. 1. (a) A depiction of the coax-line architecture includes a patterned sapphire chip (blue) inserted into a tubular enclosure and clamped at both ends (brown). Indium wire (not shown) secures the chip within the clamps. The resonator is patterned in the center of the chip, acting as the center conductor of a coaxial transmission line resonator. The enclosure ends are many attenuation lengths away from the resonator. Small red arrows represent the electric field pattern of the $\lambda/2$ resonant mode. Dashed arrows indicate the input and output paths used in transmission measurements. Coupling pins (gold), recessed within two smaller waveguides that intersect the primary enclosure, couple evanescently and carry signals to external connectors. (b) The configuration of couplers in a symmetric transmission experiment.

exponentially attenuated.

We evaluate device performance beginning with one simple element: a resonator. Choosing a quasi-stripline architecture, we pattern a $\lambda/2$ resonator on the substrate and position it near the center of the enclosure. The resonant frequency is primarily determined by the length of the conducting strip, but also depends on chip size, chip placement, and enclosure diameter.

Inspired by the robust coupling method used in 3D cavities, we introduce input and output signals using two evanescently-coupled pins within sub-cutoff waveguides that intersect the primary waveguide enclosure. Pins are recessed to an adjustable depth within each coupling enclosure, located above each end of the stripline. Both pins are used in transmission measurements (Figure 1b). Just one pin can be used to measure in reflection or feedline-coupled transmission¹³. As described later, this approach yields predictable couplings that can be varied over a wide dynamic range without compromising package integrity.

To verify that these devices are suited to complex experiments, we first demonstrate long lifetimes. For resonators, this requires achieving a high internal quality factor (Q_i) at sufficiently weak coupling (high cou-

pling quality factor Q_c). We measure these parameters by cooling coax-line resonators to ~ 20 mK and exciting single-photon-or-less circulating power. The devices are connected in a feedline-coupled configuration and transmission coefficient S_{21} is measured using a vector network analyzer (VNA). Coupling parameters are extracted from fits to S_{21} (Figure 2a inset). Measurements are usually performed in an undercoupled configuration ($Q_c \geq Q_i$, with Q_c up to 10^9) so that the total quality factor Q ($1/Q = 1/Q_i + 1/Q_c$) is a direct measure of the internal losses. The best reported Q_i for lithographically-defined aluminum-on-sapphire resonators fabricated under similar conditions (e-beam evaporation, no substrate annealing) is ~ 1 million¹⁴. We observe Q_i as high as $(8.0 \pm 0.5) \times 10^6$ at single-photon power, surpassing this by about an order of magnitude. This suggests that quality factors in lithographic devices are not solely dependent on materials or fabrication methods, but are also affected by package contributions.

By restricting wave propagation to seamless waveguides with cutoffs far above the operating frequency, we demonstrate that mode coupling can be made arbitrarily weak without additional structures or filtering¹⁵. By varying the coupling attenuation distance and measuring Q_c , we see good agreement with the expected exponential scaling over six decades with no observed upper limit (Figure 2b). Control over a large dynamic range in coupling strengths is possible by simply modifying pin length. Therefore, we can achieve very strong coupling ($Q_c \sim 10^3$) to some elements used for measurement or readout, at the same time as weak couplings ($Q_c \sim 10^8$) used to excite and control long-lived memory elements.

Another critical requirement of a properly-designed package is to prevent spurious electromagnetic modes. Using stronger coupling and a symmetric transmission configuration, we measured S_{21} to determine the spectral “cleanliness” over a large range. Because the enclosure should attenuate any modes below its cutoff frequency in the absence of package seams, we expect the measured background to be low, dominated by the noise of other elements in the measurement chain. Figure 2c shows a calibrated S_{21} trace within the measurement bandwidth of our high electron mobility transistor (HEMT) amplifier. Aside from the fundamental ($\lambda/2$) and first harmonic (λ) modes arising from the stripline resonator, no other modes are observed. This confirms that good mode control can be achieved using a coax-line architecture.

As the next step in increasing complexity, we pattern a transmon qubit alongside the resonator¹⁸. We characterize the system’s coherence and compare measured parameters to simulation. We control the qubit using a weakly-coupled port and read out through the resonator and its more strongly coupled port. These qubits exhibit 30–80 μ s lifetimes, near to the state of the art values for transmon T_1 ’s (Figure 3a). This is equivalent to quality factors ≤ 3 million, not far from those of resonators. Undercoupled resonators had equally high Q_i with and without qubits. Important system parameters, such as

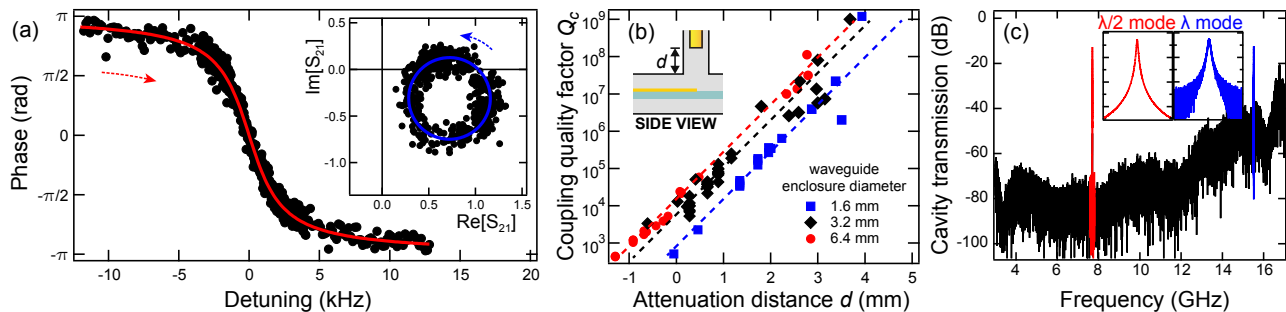


FIG. 2. (a) Resonator quality factors Q_i and Q_c are extracted from fits of the resonance circle in S_{21} (inset) and the phase response (main figure)¹⁶. Data are measured at an average cavity photon number $\bar{n} \approx 1$ where unsaturated defects produce 30–50% lower Q relative to higher powers¹⁷. A representative sample, plotted, has $Q_i = 5.98 \pm 0.07$ million and $Q_c = 4.27 \pm 0.07$ million. Dashed arrows indicate frequency sweep direction. (b) Coupling quality factor Q_c is measured for 12 mm-long resonators in enclosures with three different diameters (solid points). The attenuation distance d (inset) is measured from the end of the coupling pin to the edge of the enclosure, and enters the enclosure for $d < 0$. We measure Q_c as high as 10^9 , above which reduced SNR hinders measurement for our typical Q_i 's. Measured Q_c 's follow exponential behavior (dashed lines) with minor deviations due to resonator shape, chip placement, and machining variance. This suggests that no unknown mode couples more strongly than $Q_c = 10^9$. (c) Transmission measurements show only the expected resonant modes, here at 7.7 GHz and 15.5 GHz (insets have 300 kHz span). The fundamental mode sees isolation of > 60 dB. The noise floor is due to the frequency dependence of the readout system and HEMT noise.

mode frequencies and qubit anharmonicity, were found to agree well with predictions from finite-element simulations of the design^{13,19}. This is the first indication that additional complexity can be added to a coax-line device without decreasing control over parameters or coherence values.

The presence of a lithographic resonator-qubit system enables us to test whether on-chip element coupling follows the same waveguide-attenuated behavior as external coupling. We expect that by varying the distance z between element ends (Figure 3b inset), the chip enclosure will exponentially attenuate electric field $|\vec{E}| \propto e^{-\alpha z}$. The resonator-qubit dispersive shift χ should scale as $\chi \sim |\vec{E}|^2$. However, different resonator-qubit detunings Δ between samples make direct comparison difficult. To relate them consistently to z , we calculate an effective coupling g defined by the relation $\chi = 2g^2/\Delta$, related to the detuned Jaynes-Cummings model²⁰. When z is varied experimentally, we find that the measured change in g is consistent with a calculated waveguide attenuation scale length $1/\alpha \approx 1.02$ mm, as well as with simulations (Figure 3b). This suggests that no unintended coupling is present, and that reasonably small separations between elements can produce a range of qubit-resonator couplings useful for typical cQED applications.

The lifetimes of resonators and qubits in this system can be understood by examining the spatial participation of each mode in dissipative dielectrics and conductors. The large resonator mode volume dilutes lossy material participation—the same effect that increases coherence of 3D cavities relative to traditional planar circuits. By measuring resonators in waveguide enclosures with different diameters, we find that higher Q_i generally corresponds with larger diameter¹³. This scaling behavior is consistent with loss originating from waveguide sur-

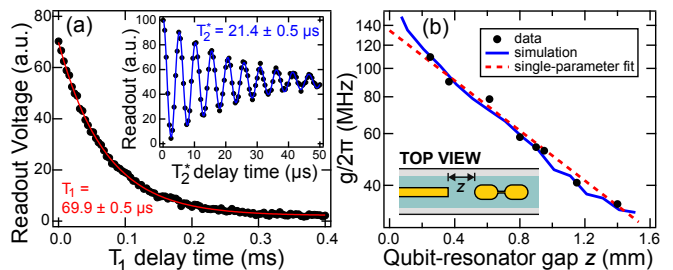


FIG. 3. (a) Qubit T_1 (main figure) and T_2^* (inset) of one characteristic device. The T_1 experiment is fit to an exponential (red), while the detuned T_2^* Ramsey experiment is fit to an exponentially decaying sine function (blue). (b) Coupling between the qubit and stripline resonator is controlled by adjusting their end-to-end separation z (inset). Values of effective qubit-stripline coupling rate g are measured for different z (black points) and fit using an exponential function $Ae^{-\alpha z}$ (dashed red line) with single free parameter A . The calculated attenuation, 8.5 dB/mm, comes from simulation of a 2.8 mm-diameter waveguide with bare substrate. A full system finite-element simulation (solid blue line) predicts similar scaling.

face resistance, a waveguide dielectric layer, or on-chip dielectric layers, but does not distinguish between these mechanisms.

Even though the enclosure body is seam-free, we can evaluate whether seams at each end introduce dissipation. We predict their effect using a model of seam loss as a distributed admittance⁶ applied to simulation. The simulation places a conservative bound, $Q_i \geq 10^8$, on typical designs separated 7 mm from the waveguide end. Positioning striplines ~ 3 mm from one end of an enclosure produced an immeasurable effect on Q_i , thereby

raising this bound. Since typical devices see significantly greater isolation from end seams, they appear unlikely to affect performance. Therefore, coax-line devices are well-positioned to act as a testbed for alternative loss mechanisms. Further studies will be required to pinpoint the dominant sources of loss, but the coherence levels already achieved allow us to increase the system's complexity further.

III. INTEGRATION AND EXPANSION

Many circuit elements must be integrated within a single enclosure to allow more versatile, hardware-efficient cQED experiments. To demonstrate an instance of a long-lived element in the presence of significant complexity, we combine a very high- Q 3D cavity with the coax-line architecture. In the resulting package (Figure 4a), the pads of a transmon qubit bridge two structures: the coax-line qubit-and-stripline system and a 3D coaxial stub cavity¹².

We characterize parameters of the complete system, including coupling and coherence values. Both the qubit and the high- Q cavity perform well, with qubit $T_1 = 110 \mu\text{s}$, qubit Ramsey decay time $T_2^* = 40 \mu\text{s}$, cavity $T_1 = 2.8 \text{ ms}$ (Figure 4b), and cavity $T_2^* = 1.5 \text{ ms}$ for the $|1\rangle$ Fock state¹². These qubit lifetimes are among the best measured in 3D cavities, and the coaxial stub resonator T_1 does not decrease when a qubit is added. This suggests that no additional sources of dissipation are introduced when these elements are combined into a single, seamless package.

Integration with 3D cavities is not strictly necessary to produce a module with many coherent circuit elements. In an all-lithographic system on a single chip, we can add components without sacrificing the isolation between non-adjacent elements. Figure 4c shows a coax-line variant with two additional stripline resonators. These resonators function as a bandpass Purcell filter^{21,22} and high- Q storage resonator. We measure coherence consistent with qubit-and-stripline designs (best qubit $T_1 \approx 60 \mu\text{s}$, $T_2^* \approx 50 \mu\text{s}$, Hahn echo decay time $T_2 \approx 60 \mu\text{s}$) and with a large cavity decay rate and qubit-readout coupling. Numerous devices were measured, producing consistently long lifetimes (Table S2). The best stripline storage resonator in this four-element module has $T_1 = 250 \mu\text{s}$, or an equivalent $Q_i = 11.2$ million. These results demonstrate that entirely chip-based designs can produce a highly coherent quantum module. A concept for how these modules could be expanded, including eight Purcell-filtered qubits and two multiplexed readout lines, is shown in Figure 4d.

IV. OUTLOOK AND CONCLUSION

We have introduced a 3D enclosure and chip-based coax-line architecture that allow for complex cQED ex-

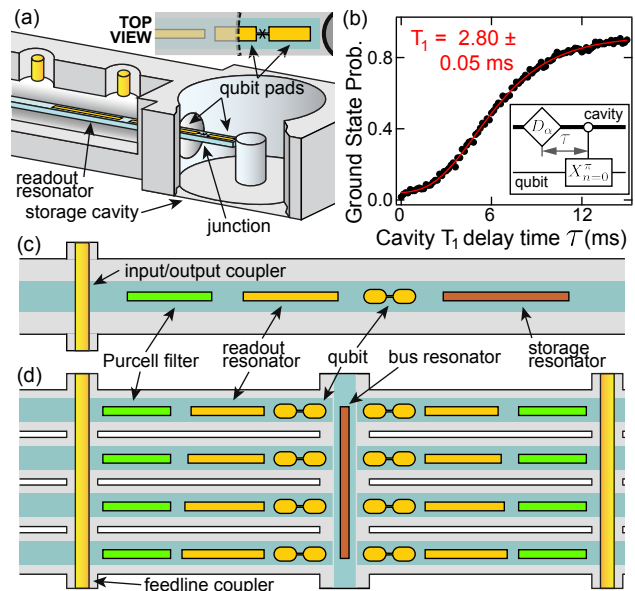


FIG. 4. (a) Combining a chip-based circuit with a 3D coaxial stub cavity. The transmon qubit antenna pads straddle the circular waveguide enclosure and stub cavity. Qubit-stripline coupling is controlled lithographically, and qubit-cavity coupling is set by antenna geometry and chip position. (b) Cavity T_1 is fit (red) to data (black points). The cavity lifetime is not spoiled by the qubit's shorter lifetime. (c) We extended the chip-based qubit-stripline system by adding a Purcell filter and high- Q stripline storage resonator. It requires a single pin-coupler in a feedline-coupled configuration. (d) We propose an expansion of multiple chip-based modules, in which eight Purcell-filtered qubits interact with a bus resonator and are addressed by two multiplexed readout lines.

periments. The device construction, absent of seams and based on natural waveguide isolation, suppresses spurious modes and allows for precisely-engineered couplings. Using undercoupled stripline resonators, we measured the highest Q_i in a chip-based cQED device to date. We integrated this type of resonator with a qubit and a millisecond 3D cavity without introducing further loss, creating a long-lived, multi-cavity cQED system. Adaptations of this system have already been used in more complex experiments with multiple qubits or cavities^{23,24}.

Using this architecture, existing designs may be improved and new capabilities created. On-chip amplification schemes could possibly be integrated with readout feedlines, allowing multiplexed single-shot readout. Many more elements could be added, producing dense multi-qubit, multi-cavity systems. The concept could apply to wafer-scale micromachining designs, where more complex, multi-layer circuits could be fabricated⁴.

This flexibility, in addition to high coherence properties, may yet inspire the next generation of hardware towards fault-tolerant error correction.

ACKNOWLEDGMENTS

We thank M. H. Devoret, J. Blumoff, K. Chou and E. Holland for helpful discussions and T. Brecht for technical assistance. This research was supported by the U.S. Army Research Office (W911NF-14-1-0011). Facilities use was supported by the Yale Institute for Nanoscience and Quantum Engineering (YINQE), the Yale SEAS cleanroom, and the NSF (MRSECDMR 1119826). C.A. acknowledges support from the NSF Graduate Research Fellowship under Grant No. DGE-1122492. K. S. acknowledges support from the Yale Science Scholars Fellowship. W. P. was supported by NSF grant PHY1309996 and by a fellowship instituted with a Max Planck Research Award from the Alexander von Humboldt Foundation.

SUPPLEMENTARY MATERIAL

S1. FABRICATION AND ASSEMBLY

Resonators were fabricated on c-plane EFG sapphire chips using photolithography, deposition of evaporated aluminum 80 nm thick, and a lift-off process. Resonators with qubits were fabricated simultaneously using electron beam lithography, bridge-free double-angle evaporation²⁵, and a lift-off process. No significant difference in Q_i was noted between resonators fabricated using the two methods. The enclosure was machined from high-purity (99.995%) aluminum and chemically etched using Aluminum Etchant A (Transene, Danvers, MA) for 4 hours. Alignment within the waveguide was achieved mechanically. Coupling pin lengths were chosen in a manner identical to that of standard 3D cavities.

S2. MEASUREMENT

Qubits were measured in transmission using asymmetric coupling (a weakly-coupled input and a strongly-coupled output port) and standard high-power readout techniques²⁶. Resonators were measured in transmission or feedline-coupled configurations. In the feedline-coupled configuration, the measurement transmission line is interrupted by a tee connected to one port of the resonator. Differing impedance in each direction as seen from the device port introduces an asymmetry in resonance lineshape. (This configuration is sometimes called “hanger” since the resonator appears to hang off the feedline.) Resonator quality factors were extracted by fitting to a complex model for S_{21} ¹⁶, accounting for impedance asymmetry, amplification and attenuation, and electrical delay. Unlike the transmission configuration, feedline-coupled measurements produce internal quality factor Q_i and coupling quality factor Q_c without knowledge of line losses. Fits were performed in two steps, as illustrated in Figure 2. The standard error for parameters in each fit

TABLE S1. Simulated and measured parameters for the resonator-qubit system corresponding with Figure 3a. The deviation of several parameters is larger than expected due to junction aging (see text). Simulation does not account for dissipation, and so the simulated κ_r represents the qubit’s Purcell limit.

Parameter	Experiment (MHz)	Simulation (MHz)	Deviation (%)
$\omega_q/2\pi$	5441.9	5828.3	6.6
$\omega_r/2\pi$	9269.5	9338.0	0.7
$\chi_{qr}/2\pi$	-2.31	-2.74	15.7
$\chi_{qq}/2\pi$	-238.5	-236.9	0.7
$\chi_{rr}/2\pi$	-	-8×10^{-3}	-
$\kappa_r/2\pi$	3.7×10^{-3}	-	-
$\kappa_q/2\pi$	1.4×10^{-2}	3.6×10^{-5}	-
p_e	2%	-	-
Parameter	Time (μ s)		
T_1	69.9		
T_2^*	21.4		
T_2	29.2		

was propagated to calculate the error in Q_i and Q_c . Measurements at higher powers helped to establish a trend in Q_i versus power with which low-power measurements were consistent. To further confirm the measured values of total quality factor, cavity ringdowns were measured following a pulsed excitation, and in the case of resonators with qubits, a cavity T_1 experiment was performed. Measurements used standard microwave lines, including a HEMT amplifier, in a dilution refrigerator with a measurement stage temperature of about 20 mK.

S3. CAVITY-QUBIT SYSTEM PARAMETERS

Table S1 includes notable device parameters. The $\kappa_{q,r}$ associated with the qubit and resonator, respectively, reflect the dissipation-free case, and can be considered the qubit’s Purcell limit and resonator’s coupling Q_c . Any addition of loss will increase these values, leading to a large “deviation”.

Simulation was generally able to predict first-order parameters within several percent of measured values. Larger deviation can be attributed to oxidation of the Josephson junction between measurement of its normal state room temperature resistance and cold measurement. This produces a discrepancy between measured and simulated qubit frequency, which propagates to other parameters. Other errors can be attributed to variability in machining, etching, and mechanical positioning. Improvement in mounting technique should improve parameter accuracy. Finite-element simulations were performed using Ansys HFSS.

Table S2 lists important measured parameters for devices of the type shown in Figure 4c. Multiple non-interacting devices were enclosed in the same package, sharing a feedline for multiplexed readout. Therefore, statistics for a relatively large number of devices were

obtained. Lower readout Q_c (higher κ_r) seems to correspond with lower values for storage cavity T_1 , consistent with possible Purcell limitation.

S4. LOSS DETERMINATION

To determine whether the resonator loss can be explained using conventional theories, we measure the quality factors (and qubit lifetimes, when present) of nearly 100 devices and performed corresponding loss simulations. We consider several likely dissipation sources, including bulk substrate dielectric, interface dielectrics, and conductor surface effects. The electric fields of both resonator and qubit modes fill similar fractions of dielectric as their analogues in standard 3D cavities, so we expect them to be limited by similar mechanisms. We refer to the fraction of the electric field energy stored in the volume labeled i as the participation ratio p_i ²⁷.

We obtain the largest dynamic range in participation by varying the diameter of waveguide enclosures with diameters ranging from about 1–6 mm. Internal quality factor are observed to increase from about 1 to 8 million as the waveguide diameter increased, and then taper off, with the largest values measured for a diameter equal to 4 mm (Figure S1). At very large diameters, reduced waveguide isolation may introduce radiative loss or increase the field’s sampling of seams at the waveguide ends. A larger mode volume is consistent with reduced electric field participation at surfaces. Unfortunately, as in former studies^{11,27,28}, loss among the contributors scales similarly between each surface as a function of enclosure diameter.

The best resonator internal quality factor, 8.0 ± 0.5 million, had a larger-than-nominal stripline width and is not included in Figure S1. For similar reasons, resonators measured on chips with qubits, including the stripline storage resonator with $Q_i = 11.3 \pm 0.3$ million, are not compared in this figure.

From the behavior of five possible contributors—the surface dielectric and conductor surface loss of (1) the enclosure aluminum and (2) the deposited aluminum and chip surfaces, plus the sapphire substrate dielectric—we determine the ones that best fit the trend and analyze them more closely. The strongest diameter-dependent scaling behavior belongs to the waveguide enclosure surface losses. We can use our participation ratios p_i to develop lower bounds on Q_{material} and compare those to established values. Conversely, we can apply the established values of Q_{material} to our p_i to obtain a lower bound on Q_i . These values are calculated in Table S3, and uses our highest measured Q_i ’s to place the most stringent bounds.

The best bound on the dielectric loss tangent of similar-quality sapphire comes from 3D qubits with lifetimes exceeding 100 μs . These qubit modes store 90% of their electric field energy in the sapphire substrate, and appear to be limited by other loss mechanisms²⁷. Ex-

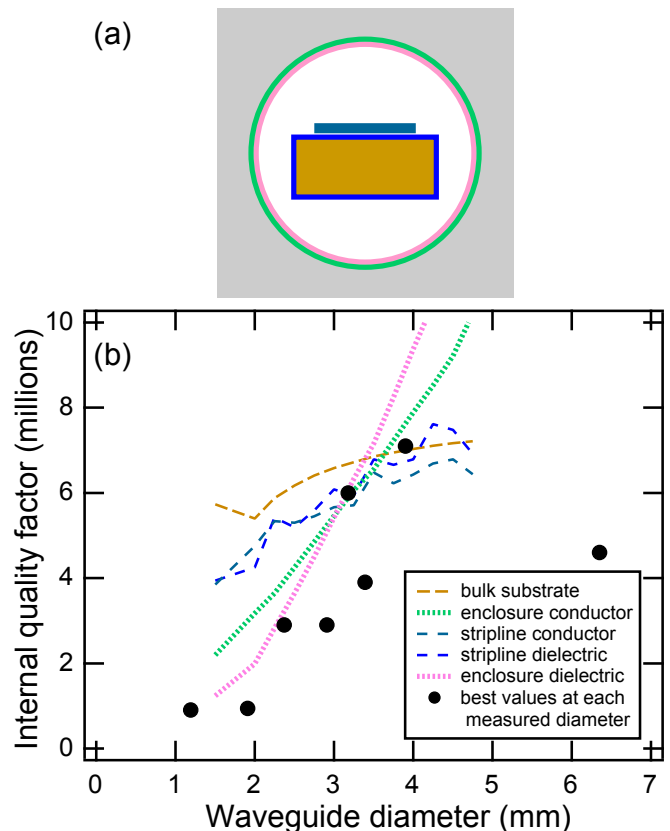


FIG. S1. (a) A schematic cross-section of the enclosure, substrate, and stripline. Sizes are exaggerated. The colored lines suggest possible dissipation sources (see text) and correspond with the legend in (b). (b) Stripline resonators with similar designs were measured in packages with different waveguide diameters. At most diameters, more than one sample was measured. The highest value at each diameter is plotted (black circles). Participation ratios p_i are simulated for several loss sources. The corresponding limiting quality factors, obtained by $Q_{\text{limit}} = Q_{\text{material}}/p_i$ for each material, are calculated and plotted using dashed or dotted lines. Each Q_{limit} trace is scaled by a value of Q_{material} to lie at or above the highest data point, representing a conservative bound. The dashed lines, relating to p_i of bulk substrate (orange), stripline conductor surface (turquoise), and stripline dielectric layers (blue), are not very consistent with the measured behavior. The dotted lines, representing the enclosure conductor surface (green) and any enclosure dielectric (pink), scale more appropriately. However, the values of Q_{material} used to scale these traces are considerably lower than the bounding values of Q_{material} determined empirically in other experiments. Noisy and jagged features in the simulated data are numerical anomalies due to difficulty of combining large 3D simulations with small planar features.

periments in separate systems with higher quality sapphire have determined even higher bounds³⁰. Table S3 shows the values obtained for our standard devices. However, by using a non-standard device, we can alter the p_i for sapphire substrate participation and place a higher bound. In one instance, we placed two stripline res-

TABLE S2. Measured parameters for separate devices containing readout cavity, qubit, Purcell filter and storage cavity as shown in Figure 4c. Qubit, storage, and readout resonant frequencies ($\omega_{q,s,r}$) as well as parameters χ and κ are divided by 2π and shown in units of MHz. Qubit coherence times T_1 , T_2^* , and T_2 are in μs , and are the average of measurements over several hours with a typical spread of $\pm 10 \mu\text{s}$. The highest individual $T_1 = 85 \mu\text{s}$, $T_2^* = 67 \mu\text{s}$, and $T_2 = 80 \mu\text{s}$. Omitted values were not measured.

Device	ω_q (MHz)	ω_s (MHz)	ω_r (MHz)	χ_{qr} (MHz)	χ_{qs} (MHz)	κ_r (MHz)	T_1 (μs)	T_2^* (μs)	T_2 (μs)	T_1^s (μs)	Q_i^s ($\times 10^6$)
1A	5509.3	6990.0	9350.9	3.10	1.84	4.14	47	28	62	37	1.63
1C	5431.1	7125.7	9406.5	-	2.00	0.34	68	26	41	143	6.40
2B	5423.7	7035.1	9377.7	2.55	1.76	4.50	43	18	47	37	1.64
2C	5362.8	7124.8	9436.1	-	1.34	0.46	51	13	78	85	3.81
3A	5573.9	7065.5	9447.5	2.38	1.85	2.88	62	9	51	121	5.37
3B	5345.8	7066.2	9442.8	2.47	1.59	2.15	62	49	59	91	4.04
3C	5378.8	7160.7	9493.3	-	1.58	1.02	72	23	69	250	11.25
4A	5551.2	7093.6	9464.7	2.64	1.97	5.43	55	33	41	112	4.99
4B	5417.2	7098.2	9475.0	1.60	1.59	5.89	41	15	56	121	5.40
4C	5269.8	7158.0	9511.7	-	1.35	0.27	13	0.2	4	154	6.93
5A	5672.8	7108.0	9542.1	1.62	1.97	9.47	23	21	20	25	1.12
5B	5540.8	7098.0	9536.0	0.08	1.68	8.65	26	18	21	66	2.94
5C	5459.6	7228.0	9607.2	-	1.67	2.57	36	14	33	154	6.99

TABLE S3. Simulated and measured values for system dissipation sources. Values of Q_{material} are lower bounds and are obtained from single-photon measurements of similar systems. Our range of participations p_i are obtained from simulation, except for conductor participation (where $p_i = \alpha$, kinetic inductance fraction), which is measured. The calculation of our Q_{material} comes from the best measured $Q_i = 8$ million, while the calculated Q_i limit is a product of the established Q_{material} bound and $1/p_i$.

Source	established Q_{material} bound	Q_{material} source	our p_i	our Q_{material} bound	our Q_i limit $\times 10^6$
Substrate sapphire	$1-5 \times 10^6$	3D qubits ^{10,29} , WGMR ³⁰	0.4–0.5	3.2×10^6	2.0–12.5
Enclosure conductor	4400	cylindrical cavity ³¹	$1-10 \times 10^{-6}$	8	440–4400
Stripline conductor	4800	AI WGMR ³²	$1-4 \times 10^{-3}$	8000	1.2–4.8
Stripline dielectric interfaces	380	3D qubits ²⁷	$1-3 \times 10^{-5}$	80	13–38
Enclosure dielectric	750	coaxial stub cavity ¹²	8×10^{-7}	6.4	940

onators side-by-side on the same substrate. In another, the two resonators were patterned on the front and back of the substrate. These variations allowed a differential and a common mode with significantly different p_i , ranging from 24–89%. For each device, the mode with higher sapphire participation exhibited a Q_i about 50% higher than the opposite mode. This inverse relationship does not identify the dominant loss source, but does seem to rule out our substrate material.

Next, we considered the kinetic inductance fraction α —a metric of dissipation within the superconductor—and measured its effect using the dependence of resonant frequency on temperature³¹. Repeating this experiment with striplines made from higher- T_c niobium, we obtained the α of the waveguide enclosure independently. Our standard design resulted in $\alpha = 1-4 \times 10^{-3}$ for the stripline and $\alpha = 10^{-6}-10^{-5}$ for the waveguide enclosure. Using the established Q_{material} bound on etched high-purity bulk aluminum³¹ we place a conservative lower limit on Q_i due to waveguide surface dissipation at 4×10^8 . Even though the diameter-dependent behavior of waveguide conductor surface loss in Figure S1 matches well with measured Q_i , it seems highly unlikely that this is the limiting loss source based on formerly established

bounds.

We consider thin-film deposited aluminum separately, since it undergoes fundamentally different processing. Here, the best published bounds³² predict this loss mechanism to be strongly limiting. However, an updated study has established significantly higher bounds³³. Additionally, the value of α is not measured to change significantly as waveguide diameter is varied, and so cannot explain the measured changes in Q_i with diameter.

Loss contribution from surface dielectric interfaces (at the metal-substrate, substrate-vacuum, or metal-vacuum interfaces) remain a plausible limit. The best established limit on those surfaces²⁷ is within an order of magnitude of our value. However, as with the other surface effects, the diameter-dependent scaling is not consistent with measured Q_i . This comparison is further obscured by the fact that the relative contribution of these three primary surfaces cannot be empirically differentiated.

While no single source conclusively dominates the loss in our system, we may be limited by many sources contributing at similar levels. Alternatively, we may be affected by loss from an unconsidered source, such as vortices, mechanical dampening, or substrate processing. The strong dependence of Q_i on waveguide diameter is

suggestive of a non-localized material dissipation, and is consistent with prior observations of Q_i proportional to mode volume in cQED systems. The ability of this system to controllably evaluate on-chip and package losses independently, to some degree, lends versatility to the design as a testbed for losses. Future studies may be able to place and raise these bounds more definitively.

REFERENCES

- ¹R. Barends, J. Kelly, A. Megrant, A. Veitia, D. Sank, E. Jeffrey, T. C. White, J. Mutus, A. G. Fowler, B. Campbell, Y. Chen, Z. Chen, B. Chiaro, A. Dunsworth, C. Neill, P. O'Malley, P. Roushan, A. Vainsencher, J. Wenner, A. N. Korotkov, A. N. Cleland, and J. M. Martinis, *Nature* **508**, 500 (2014).
- ²A. M. Steane, *Physical Review A* **68**, 042322 (2003).
- ³J. M. Gambetta, J. M. Chow, and M. Steffen, arXiv:1510.04375 [quant-ph] (2015).
- ⁴T. Brecht, W. Pfaff, C. Wang, Y. Chu, L. Frunzio, M. H. Devoret, and R. J. Schoelkopf, *npj Quantum Information* **2**, 16002 (2016).
- ⁵Z. Chen, A. Megrant, J. Kelly, R. Barends, J. Bochmann, Y. Chen, B. Chiaro, A. Dunsworth, E. Jeffrey, J. Y. Mutus, P. J. J. O'Malley, C. Neill, P. Roushan, D. Sank, A. Vainsencher, J. Wenner, T. C. White, A. N. Cleland, and J. M. Martinis, *Applied Physics Letters* **104**, 052602 (2014).
- ⁶T. Brecht, M. Reagor, Y. Chu, W. Pfaff, C. Wang, L. Frunzio, M. H. Devoret, and R. J. Schoelkopf, *Applied Physics Letters* **107**, 192603 (2015).
- ⁷G. Kirchmair, B. Vlastakis, Z. Leghtas, S. E. Nigg, H. Paik, E. Ginossar, M. Mirrahimi, L. Frunzio, S. M. Girvin, and R. J. Schoelkopf, *Nature* **495**, 205 (2013).
- ⁸M. H. Devoret and R. J. Schoelkopf, *Science* **339**, 1169 (2013).
- ⁹N. H. Nickerson, J. F. Fitzsimons, and S. C. Benjamin, *Physical Review X* **4**, 041041 (2014).
- ¹⁰H. Paik, D. I. Schuster, L. S. Bishop, G. Kirchmair, G. Catelani, A. P. Sears, B. R. Johnson, M. J. Reagor, L. Frunzio, L. I. Glazman, S. M. Girvin, M. H. Devoret, and R. J. Schoelkopf, *Physical Review Letters* **107**, 240501 (2011).
- ¹¹O. Dial, D. T. McClure, S. Poletto, J. M. Gambetta, D. W. Abraham, J. M. Chow, and M. Steffen, arXiv:1509.03859 [cond-mat, physics:quant-ph] (2015).
- ¹²M. Reagor, W. Pfaff, C. Axline, R. W. Heeres, N. Ofek, K. Sliwa, E. Holland, C. Wang, J. Blumoff, K. Chou, M. J. Hatridge, L. Frunzio, M. H. Devoret, L. Jiang, and R. J. Schoelkopf, arXiv:1508.05882 [cond-mat, physics:quant-ph] (2015).
- ¹³See supplemental material for experimental details.
- ¹⁴A. Megrant, C. Neill, R. Barends, B. Chiaro, Y. Chen, L. Feigl, J. Kelly, E. Lucero, M. Mariantoni, P. J. J. O'Malley, D. Sank, A. Vainsencher, J. Wenner, T. C. White, Y. Yin, J. Zhao, C. J. Palmström, J. M. Martinis, and A. N. Cleland, *Applied Physics Letters* **100**, 113510 (2012).
- ¹⁵M. Sandberg, M. R. Vissers, T. A. Ohki, J. Gao, J. Aumentado, M. Weides, and D. P. Pappas, *Applied Physics Letters* **102**, 072601 (2013).
- ¹⁶M. S. Khalil, M. J. A. Stoutimore, F. C. Wellstood, and K. D. Osborn, *Journal of Applied Physics* **111**, 054510 (2012).
- ¹⁷J. Gao, M. Daal, A. Vayonakis, S. Kumar, J. Zmuidzinas, B. Sadoulet, B. A. Mazin, P. K. Day, and H. G. Leduc, *Applied Physics Letters* **92**, 152505 (2008).
- ¹⁸M. Devoret, S. Girvin, and R. Schoelkopf, *Annalen der Physik* **16**, 767 (2007).
- ¹⁹S. E. Nigg, H. Paik, B. Vlastakis, G. Kirchmair, S. Shankar, L. Frunzio, M. H. Devoret, R. J. Schoelkopf, and S. M. Girvin, *Physical Review Letters* **108**, 240502 (2012).
- ²⁰A. Wallraff, D. I. Schuster, A. Blais, L. Frunzio, R.-S. Huang, J. Majer, S. Kumar, S. M. Girvin, and R. J. Schoelkopf, *Nature* **431**, 162 (2004).
- ²¹M. D. Reed, B. R. Johnson, A. A. Houck, L. DiCarlo, J. M. Chow, D. I. Schuster, L. Frunzio, and R. J. Schoelkopf, *Applied Physics Letters* **96**, 203110 (2010).
- ²²E. Jeffrey, D. Sank, J. Mutus, T. White, J. Kelly, R. Barends, Y. Chen, Z. Chen, B. Chiaro, A. Dunsworth, A. Megrant, P. O'Malley, C. Neill, P. Roushan, A. Vainsencher, J. Wenner, A. Cleland, and J. M. Martinis, *Physical Review Letters* **112**, 190504 (2014).
- ²³K. Chou, J. Blumoff, M. Reagor, C. Axline, R. Brierley, S. Nigg, P. Reinhold, R. W. Heeres, C. Wang, K. Sliwa, A. Narla, M. J. Hatridge, L. Jiang, M. H. Devoret, S. M. Girvin, and R. J. Schoelkopf, (in preparation).
- ²⁴C. Wang, Y. Y. Gao, P. Reinhold, R. W. Heeres, N. Ofek, K. Chou, C. Axline, M. Reagor, J. Blumoff, K. M. Sliwa, L. Frunzio, S. M. Girvin, L. Jiang, M. Mirrahimi, M. H. Devoret, and R. J. Schoelkopf, *Science* (in press).
- ²⁵F. Lecocq, I. M. Pop, Z. Peng, I. Matei, T. Crozes, T. Fournier, Cécile Naud, W. Guichard, and O. Buisson, *Nanotechnology* **22**, 315302 (2011).
- ²⁶M. Reed, *Entanglement and Quantum Error Correction with Superconducting Qubits*, Ph.D. Thesis, Yale University (2013).
- ²⁷C. Wang, C. Axline, Y. Y. Gao, T. Brecht, Y. Chu, L. Frunzio, M. H. Devoret, and R. J. Schoelkopf, *Applied Physics Letters* **107**, 162601 (2015).
- ²⁸M. Sandberg, M. R. Vissers, J. S. Kline, M. Weides, J. Gao, D. S. Wisbey, and D. P. Pappas, *Applied Physics Letters* **100**, 262605 (2012).
- ²⁹C. Rigetti, J. M. Gambetta, S. Poletto, B. L. T. Plourde, J. M. Chow, A. D. Córcoles, J. A. Smolin, S. T. Merkel, J. R. Rozen, G. A. Keefe, M. B. Rothwell, M. B. Ketchen, and M. Steffen, *Physical Review B* **86**, 100506 (2012).
- ³⁰D. L. Creedon, Y. Reshitnyk, W. Farr, J. M. Martinis, T. L. Duty, and M. E. Tobar, *Applied Physics Letters* **98**, 222903 (2011).
- ³¹M. Reagor, H. Paik, G. Catelani, L. Sun, C. Axline, E. Holland, I. M. Pop, N. A. Masluk, T. Brecht, L. Frunzio, M. H. Devoret, L. Glazman, and R. J. Schoelkopf, *Applied Physics Letters* **102**, 192604 (2013).
- ³²Z. K. Mineev, I. M. Pop, and M. H. Devoret, *Applied Physics Letters* **103**, 142604 (2013).
- ³³K. Serniak and M. H. Devoret (in preparation).